Tuning the structure of the skyrmion lattice system Cu$_2$OSeO$_3$ under pressure

Srishti Pal [1], Pallavi Malavi [1], Shashank Chaturvedi,[2,3] Subhadip Das [1], S. Karmakar [4], D. V. S. Muthu [1],
Umesh V. Waghmare,[3] and A. K. Sood [1,*]

[1]*Department of Physics, Indian Institute of Science, Bengaluru, 560012, India*
[2]*Chemistry and Physics of Materials Unit, School of Advanced Materials,*
Jawaharlal Nehru Centre for Advanced Scientific Research, Bengaluru, 560064, India
[3]*Theoretical Sciences Unit, School of Advanced Materials,*
Jawaharlal Nehru Centre for Advanced Scientific Research, Bengaluru, 560064, India
[4]*High Pressure and Synchrotron Radiation Physics Division, Bhabha Atomic Research Centre, Trombay, Mumbai 400085, India*

The insulating ferrimagnet Cu$_2$OSeO$_3$ shows a rich variety of phases such as skyrmion lattice and helical magnetism controlled by interplay of different exchange interactions which can be tuned by external pressure. In this work we have investigated pressure-induced phase transitions at room temperature using synchrotron-based x-ray diffraction and Raman-scattering measurements. With first-principles theoretical analysis, we show that spin-spin exchange couplings in the ambient cubic phase are affected notably by hydrostatic pressure. The ambient cubic phase transforms to a monoclinic phase above 7 GPa and then to the triclinic phase above 11 GPa. Emergence of new phonon modes in the Raman spectra confirms these structural phase transitions. Notably, upon decompression, the crystal undergoes a transition to a new monoclinic structure. Atomic coordinates have been refined in the low-pressure cubic phase to capture the Cu-tetrahedra evolution responsible for the earlier reported magnetic behavior under pressure. Our experiments will motivate further studies of its emergent magnetic behavior under pressure.

I. INTRODUCTION

Cu$_2$OSeO$_3$ belongs to an interesting family of chiral, non-centrosymmetric B20 magnetic systems that host a unique magnetic phase diagram consisting of helical, conical, and skyrmion lattice structures [1,2]. Among mostly intermetallic systems like MnSi [3,4], Fe$_{1-x}$Co$_x$Si [5] and FeGe [6], Cu$_2$OSeO$_3$ is the first insulating material of this family that has been intensively studied for the rich physics of its skyrmion lattice phase [1]. A skyrmion is a few-nanometer-sized particle-like excitation emerging due to correlated spins in a vortex-like configuration [7,8] and has been realized experimentally using Lorentz transmission electron microscopy [9], reciprocal-space imaging by small angle neutron scattering [10], spin-resolved scanning tunneling microscopy [11], as well as theoretical studies [12].

Bulk Cu$_2$OSeO$_3$ crystallizes in the same P2$_1$3 cubic structure as the other B20 materials with a unit cell containing eight formula units [13]. The crystal is comprised of corner-sharing distorted Cu$_4$-tetrahedra (along the body diagonal) of two crystallographically distinct Cu^{2+} ion sites: Cu1 at 4a and Cu2 at 12b with Cu1 : Cu2 ratio of 1 : 3 serving as the backbone of magnetism in the system. It has been shown theoretically that the ground-state wave function is highly entangled and cannot be factorized into individual spin 1/2 sites [14]. The lack of inversion symmetry of the cubic

B20 crystal structure results in large Dzyaloshinskii-Moriya exchange interaction (D) and together with the Heisenberg exchange (J), it results in the development of helical magnetic ordering. Cu$_2$OSeO$_3$ possess a helical spin ground state below $T_C = 58.8$ K at zero magnetic field with a fixed pitch of ≈ 50 nm [1]. This helical ground state further develops into a skyrmion lattice phase upon applying moderate external magnetic field followed by a conical spin texture ($B > B_{C1}$) and finally to the field-polarized ferrimagnetic order at much higher field values ($B > B_{C2}$) [15]. The skyrmion lattice phase is a narrow pocket in the temperature-magnetic field phase space and its formation, size, and stability is controlled by different magnetic exchange interactions such as Heisenberg exchange, Dzyaloshinskii-Moriya exchange, and magneto crystalline anisotropy. The strengths of these interactions mainly depend on the interatomic bond parameters which can be tuned by chemical doping, disorder, or pressure. The metallic members of the B20 family, MnSi, MnGe, FeGe, and Fe$_{1-x}$Co$_x$Si, have been well studied for the pressure-induced suppression of their ordering temperature T_C which tends to absolute zero at the critical pressures of 1.5, 23, 18.8, and 7–12 GPa, respectively, above which a non-Fermi liquid (NFL) type dependence of resistivity is observed [16–19]. However, none of the above-mentioned behavior is associated with any structural deformation since the cubic symmetry of these B20 chiral magnets remain intact up to 30 GPa [19–22]. In contrast with the above itinerant magnets, T_C of the insulating Cu$_2$OSeO$_3$ increases with pressure at the rate 0.3 K/kbar [23] and this contrasting behavior has

*asood@iisc.ac.in

been attributed to the difference in the nature of the magnetic moments in these systems. Interestingly, hydrostatic pressure is found to expand the size of the skyrmion pocket in T-H phase diagram of Cu_2OSeO_3 [24]. This is due to the interplay of complex magnetic interactions that modify the exchange interaction paths in the Cu_2OSeO_3 lattice. Hence, it becomes important to study the structural stability of Cu_2OSeO_3 under pressure in order to understand its interesting magnetic properties. A recent high-pressure study by Deng *et al.* [25] shows substantial enhancement of the skyrmion pocket of Cu_2OSeO_3 reaching a vast range of 5–300 K with the upper and lower limits being achieved at pressures of 7.9 and 26.2 GPa, respectively. The authors also showed that these magnetic transitions in Cu_2OSeO_3 are associated with a series of structural modulations of the cubic symmetry through orthorhombic, monoclinic, and triclinic phases. However, the detailed structural correlation to magnetic properties is still lacking. Our study is focused on structural and vibrational evolution of Cu_2OSeO_3 under pressure, which is important in order to understand the interesting magnetic properties. The detailed structural evolution will provide valuable information for a modeling of the magnetic couplings in these systems under pressure.

II. EXPERIMENTAL DETAILS

Polycrystalline samples of Cu_2OSeO_3 were prepared by standard solid-state reaction [26]. A stoichiometric mixture of high purity CuO and SeO_2 powders was processed into a pellet, sealed in an evacuated quartz tube, and heated to 600 °C for 12 h. The process was repeated with intermediate grinding to obtain single-phase high-purity single crystals of size ≈50–500 microns.

Crystals of Cu_2OSeO_3 were finely powdered and loaded inside Mao Bell type and symmetric diamond-anvil cells (DACs) for Raman and XRD measurements, respectively. Both the DACs had two 16-facet brilliant cut diamonds with ≈600 μm culet diameter. A 4 : 1 methanol-ethanol mixture with a freezing pressure of ≈10.4 GPa [27] was used to transmit the pressure to the sample placed inside the stainless-steel gasket hole of ≈200 μm diameter. Ruby fluorescence was used to calibrate the applied pressure [28].

The pressure evolution of the Cu_2OSeO_3 crystal structure was carried out at Elettra, Italy using the Xpress beamline ($\lambda = 0.4957$ Å) at room temperature. Data were collected by using a MAR 345 image plate. A standard LaB_6 crystal was used to calibrate sample to detector distance and orientation angles of the detector. The selected area two-dimensional (2D) diffraction pattern was processed by using Fit2D software [29] for conversion into intensity vs 2θ plot. The raw data were refined and fit by using a standard Rietveld refinement procedure for the low-pressure cubic phase (up to 7.3 GPa) and the decompression data at 3.4 GPa and using the LeBail method for the rest of the pressure range in the GSAS software package [30].

The unpolarized Raman spectra at room temperature were recorded in a backscattering geometry by using the Horriba LabRAM HR Evolution Spectrometer equipped with a thermoelectric cooled charge coupled device (CCD) (HORIBA Jobin Yvon, SYNCERITY 1024 X 256). The spectra were
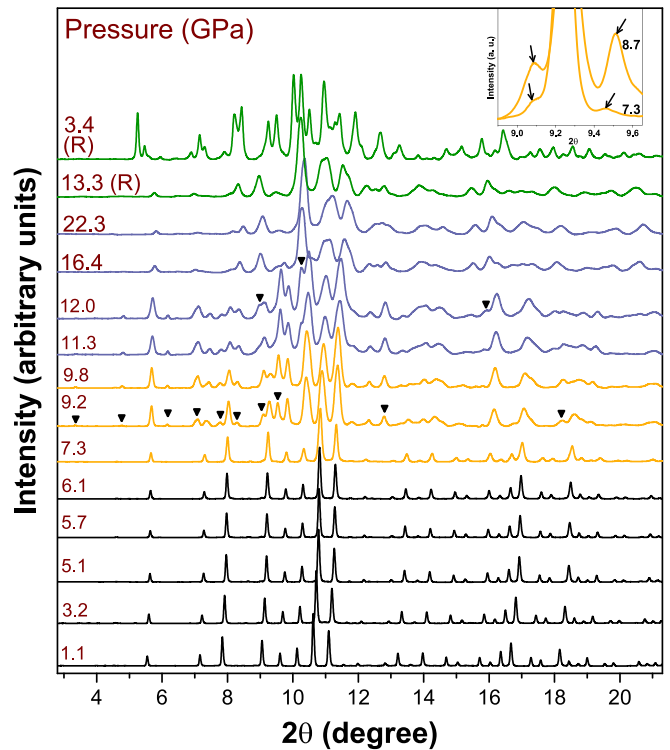

FIG. 1. Angle dispersive x-ray diffraction patterns of Cu_2OSeO_3 at selected pressures ranging from 1.1 to 22.3 GPa (the top-most pattern is after depressurizing to 3.4 GPa). Arrows indicate the appearance of new peaks. The onset of the first structural transition at 7.3 GPa is indicated in the inset.

recorded by using a 532 nm DPSS laser illuminating the sample with ≈1.5 mW power.

III. RESULTS AND DISCUSSIONS

A. X-ray diffraction

Angle dispersive powder XRD patterns of Cu_2OSeO_3 at varying pressure values at room temperature are shown in Fig. 1. The ambient cubic phase with $P2_13$ (SG : 198, $z = 8$) space group shows stability up to ≈7 GPa, above which new Bragg reflections emerge in the diffraction pattern (≈3.3°, 4.8°, 6.1°, 7.1°, 7.8°, 8.3°, 9.1°, 9.5°, 12.8°, 18.2°, and more). Appearance of new Bragg peaks over the existing ones suggests the onset of a pressure-induced first-order structural transition. The new phase has been successfully indexed to be monoclinic with space group $P12_11$ (SG : 4, $z = 8$) that coexists with cubic phase up to ≈9 GPa. The transition completes at ≈10 GPa followed by another structural transformation around 11 GPa. The phase above 11 GPa has been indexed to have triclinic symmetry with space group $P1$ (SG : 1, $z = 8$) and is found to be stable up to 22.3 GPa (the highest pressure achievable in our XRD experiment). Our results contrast with the high-pressure XRD measurements up to 10.47 GPa by Deng *et al.* [25] showing occurrence of intermediate orthorhombic phase between 5 to 7 GPa. A possible reason behind this discrepancy is the nonhydrostatic environment above ≈3 GPa offered by silicone oil [31], which is used as the pressure-transmitting medium in the high-pressure

XRD measurements by Deng *et al.* [25]. The XRD patterns shown in Fig. 1 clearly demonstrate the robustness of the cubic phase in the pressure range of 5 to 7 GPa and hence substantiates the absence of any intermediate orthorhombic phase. The structural transitions in Cu_2OSeO_3 are found to be path dependent, as indicated by the two top-most patterns of Fig. 1. The irreversibility of the structural transitions of Cu_2OSeO_3 has recently been observed in the high-pressure Raman measurements [25], although proper identification of the new phase after decompressing back to ambient was not explored. Figure 1 shows that the high-pressure triclinic phase is stable upon decompression down to 13.3 GPa, below which the system adapts a different structural transformation channel achieving a metastable monoclinic phase with space group $P12_1/c1$ (SG : 14, $z = 4$) (earlier reported by Effenberger *et al.* [32] to be a polymorph of ambient Cu_2OSeO_3) with a small fraction (17% in weight) of the cubic $P2_13$ one.

Considering the arrangements of Cu-polyhedra in the unit cell, this pressure-released monoclinic structure is in sharp contrast with the cubic polymorph as well as the high-pressure monoclinic and triclinic phases, which are derivatives of the ambient cubic structure with increased lattice distortion but similar polyhedral environment. While the cubic structure has two types of distorted CuO_5 polyhedra viz. trigonal bipyramidal around Cu1 and square pyramidal around Cu2, the monoclinic polymorph contains distorted square planar CuO_4 around Cu1 and Cu2 (at Wyckoff sites 2b and 2a) and distorted CuO_6 octahedra around Cu3 (at Wyckoff site 4e). The different Cu-Cu distances and Cu-O-Cu angles in the polymorphs are indicative of variation in the magnetic exchange interaction and so the magnetic ordering in these two polymorphic phases. Figure 2 shows fitted patterns at 1.1, 10.5, 12.7, and 3.4 (return) GPa using cubic $P2_13$, monoclinic $P12_11$, triclinic $P1$ and mixture of cubic $P2_13$ and monoclinic $P12_1/c1$, respectively. The low R_P values confirm the goodness of fit using the unit cells mentioned in the insets of Fig. 2. The refined lattice parameters for the different phases are listed in Table I.

The pressure variation of the lattice parameters in different structural phases of Cu_2OSeO_3 is shown in Fig. 3(a) with the monoclinic and triclinic angles in the inset. The different axes in the monoclinic and triclinic phase show different compressional behavior addressing the anisotropic nature of these symmetry-reduced crystal systems. The rapidly falling triclinic β_T compared with the monoclinic β_M and the
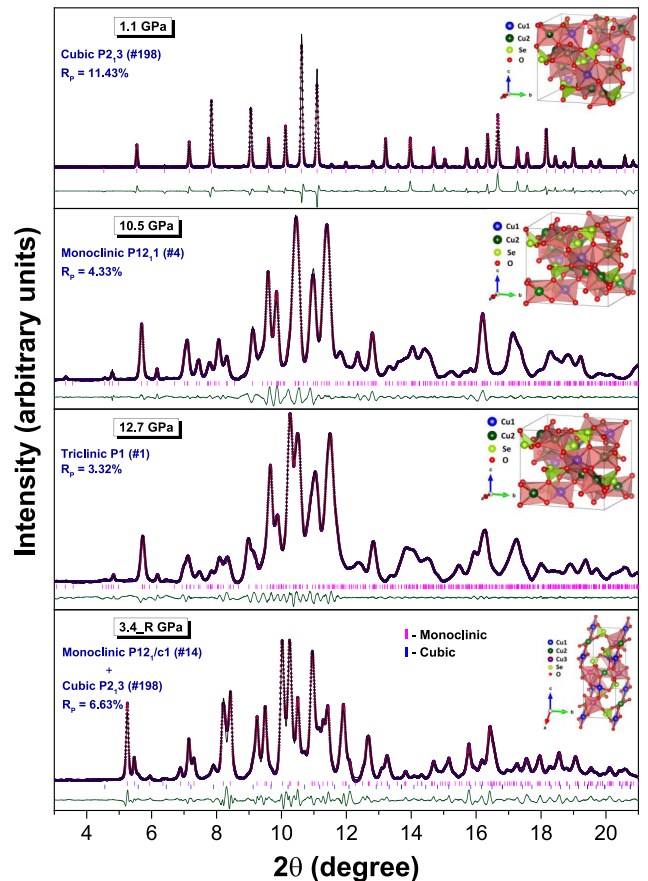

FIG. 2. Fitted XRD patterns at selected pressures with the unit cells containing the atoms shown in the insets. Experimental data are indicated by solid circles. Calculated patterns are drawn as black solid lines. Reflection positions are indicated by vertical bars. Lower dark green curves are the weighted differences between observed and calculated profile.

contrasting increments in α_T and γ_T manifest the increasing disorder in the high-pressure triclinic phase. In Fig. 3(b), the volume of the unit cell per formula unit is plotted against pressure and the data in different ranges are fit with a third-order Birch-Murnaghan equation of state (EOS) [33]. The finite-volume discontinuities across the transition pressures of ≈ 7 and ≈ 11 GPa in the P-V diagram confirm the first-order nature of these structural transitions. The volume data of the

TABLE I. Refined Lattice Parameters for different phases of Cu_2OSeO_3.

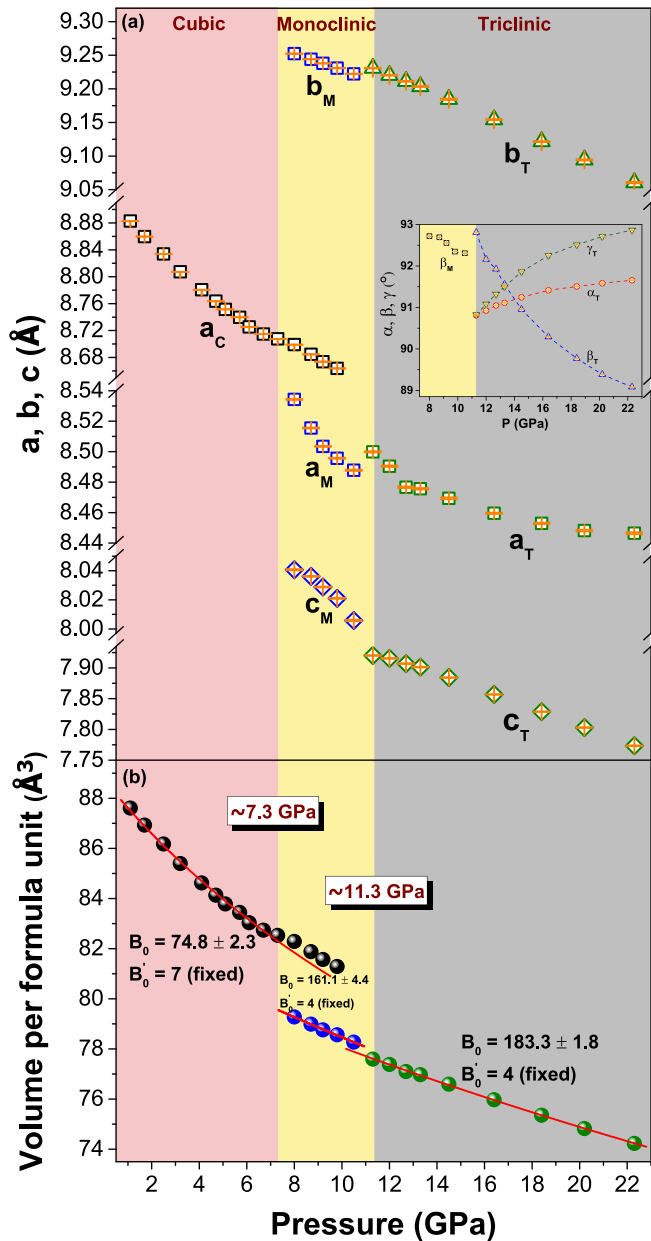|	Cubic (1.1 GPa)	Monoclinic (10.5 GPa)	Triclinic (12.7 GPa)	Monoclinic (3.4 GPa_R)
Space Group	$P2_13$	$P12_11$	$P1$	$P12_1/c1$
a, b, c (Å)	$a = 8.88921 = b = c$	$a = 8.487775$, $b = 9.222242$, $c = 8.005783$	$a = 8.499870$, $b = 9.230770$, $c = 7.920129$	$a = 6.926283$, $b = 5.868629$, $c = 10.561576$
α, β, γ (°)	$\alpha = \beta = \gamma = 90$	$\alpha = \gamma = 90$, $\beta = 92.307$	$\alpha = 90.809$, $\beta = 92.809$, $\gamma = 90.825$	$\alpha = \gamma = 90$, $\beta = 128.595$
V/f.u. (Å³)	87.801 ($z = 8$)	78.269 ($z = 8$)	77.594 ($z = 8$)	83.883 ($z = 4$)

FIG. 3. (a) Pressure dependence of lattice parameters in cubic (shaded pink), mixed phase (up to 10 GPa) of cubic and monoclinic (shaded yellow) and triclinic (shaded gray) phases of Cu_2OSeO_3, and (b) fitted (red solid line) P-V diagram using third-order BM equation of state.

cubic phase up to 7.3 GPa (before onset of the mixed phase) is used for fitting, giving values of zero-pressure volume $V_0 = 88.7 \pm 0.1$ Å^3, bulk modulus $B_0 = 74.8 \pm 2.3$ GPa with its pressure-derivative B'_0 fixed at 7. The values of V_0 and B_0 for the monoclinic phase are 82.9 ± 0.1 Å^3, 161.1 ± 4.4 GPa and for the triclinic phase are 82.0 ± 0.05 Å^3, 183.3 ± 1.8 GPa, with fixed $B'_0 = 4$. Increasing values of bulk modulus in successive phases indicate pressure hardening of the crystal.

Pressure evolution of the distorted copper tetrahedra of Cu_2OSeO_3 [Fig. 4(a)] in the cubic phase is illustrated in Figs. 4(b)–4(d) in terms of interatomic distances of Cu1 and Cu2. Both the intra- and intertetrahedral Cu-Cu distances

decrease monotonically with pressure but with different rates, indicating increasing anisotropy in the system. Figure 4(d) represents the quantitative increment in anisotropy in terms of the increasing ratio of Cu1-Cu2 and Cu2-Cu2 distances as a function of pressure. While the dominating superexchange interaction between Cu1 and Cu2 is attributed to the strong D-M interaction giving rise to exceptionally large $|D/J|$ value of 1.95, ferromagnetic Heisenberg exchange prevails between the Cu2 ions ($|D/J| \approx 0.39$) [34]. The size of the skyrmion pocket of Cu_2OSeO_3 increases with the parameter JK/aD^2 (where a is the interatomic distance, and K is the anisotropy) [24], whereas the value of the helimagnetic transition temperature T_C is directly proportional to J [35]. In the next section, with the help of extensive density-functional theory calculations, we show how the skyrmion pocket and T_C evolve with increasing pressure. After transition to the monoclinic phase, anisotropy K in the system further increases and the Cu$_4$ tetrahedra becomes more distorted, generating several unequal intra- and intertetrahedral Cu2-Cu2 and Cu1-Cu2 distances and thus detailed microscopic calculations based on our observed structural evolution are needed to explore the nature of the magnetic interactions in the high-pressure monoclinic and triclinic phases of the material.

B. Theoretical analysis

We now present results of first-principles density-functional theory (DFT) calculations to estimate various spin-coupling parameters employing VASP package [36,37]. The Hubbard parameter ($U = 7.5$ eV) was used to include electron correlations on Cu sites along with J parameter (0.98 eV), based on the method described by Liechtenstein *et al.* [38]. A generalized gradient approximation [39] (GGA) of the electron exchange-correlation energy and projector augmented wave potentials [40] were used in our calculations. The plane-wave cutoff energy was set to 500 eV. To determine the Dzyaloshinskii–Moriya vector $\boldsymbol{D}_{ij}$, we performed fully relativistic calculations with spin-orbit coupling (SOC) to determine total energies of various noncollinear spin configurations, as proposed by Xiang *et al.* [41]. To understand the nature of skyrmions, we estimate the symmetric exchange (J_{ij}) and antisymmetric exchange (D_{ij}) parameters. J-parametrized interactions give relative stability of collinear magnetic configurations with parallel and antiparallel alignment of spins, while the antisymmetric exchange parameter D stabilizes spin canting. The calculated lattice parameter of Cu_2OSeO_3 is 9.01 Å, which is 0.9% overestimated with respect to experimental value of 8.925 Å [32], well within the typical DFT errors.

The different inter- and intratetrahedral Heisenberg couplings of the Cu_2OSeO_3 unit cell are shown in Fig. 5. Our estimates of J and D parameters at 0 GPa are in agreement with earlier work (Table II) [34]. Pressure does not have same effect on all J-coupling constants (Table III). J_3 coupling weakens with pressure, which corresponds to intertetrahedral ferromagnetic coupling between Cu2 atoms, while other J interactions are enhanced with pressure. J_5, the super-superexchange interaction, exhibits a weak increase from 0 to 6 GPa. Our calculated value of $|D_4/J_4|$ at 0 GPa is 1.86, which is close to the value of 1.95 reported earlier [34]. Application
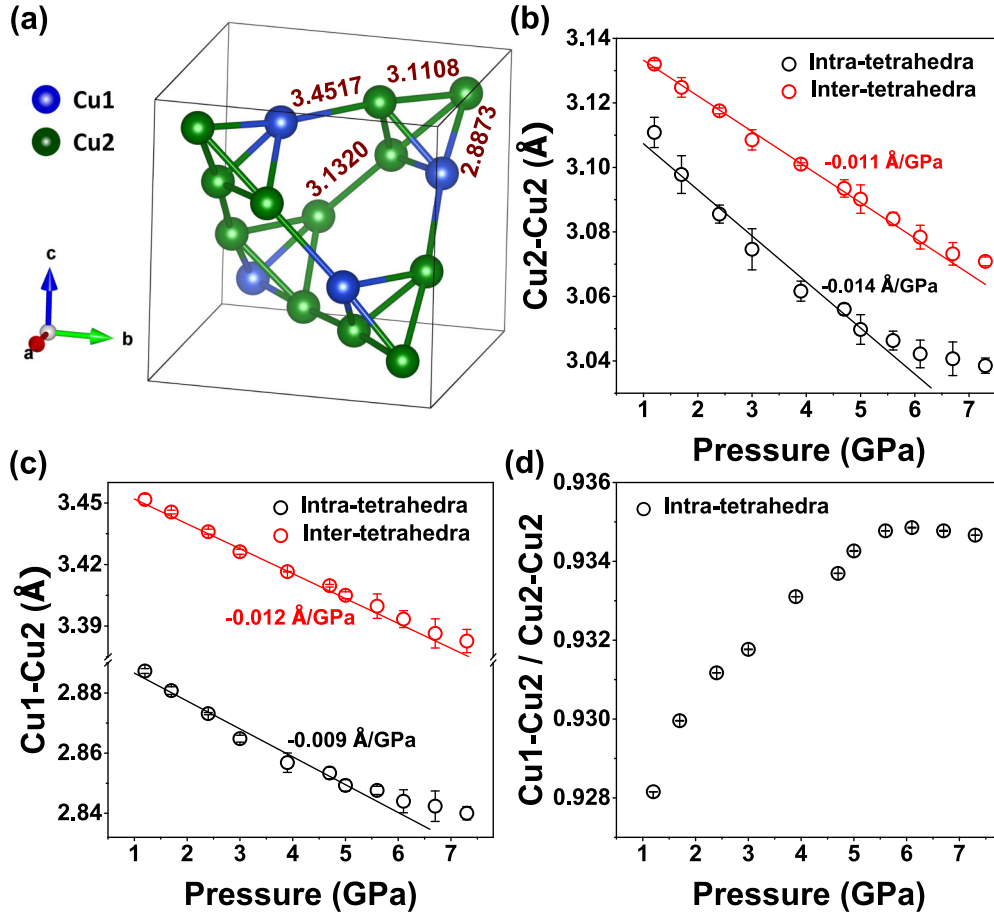
FIG. 4. (a) Unit cell of Cu_2OSeO_3 containing the Cu tetrahedra, (b) Cu2-Cu2 and (c) Cu1-Cu2 distances, (d) intratetrahedron Cu1-Cu2/Cu2-Cu2 ratio as a function of pressure in the cubic phase of Cu_2OSeO_3.

of pressure results in a reduction of $|D_4/J_4|$ to nearly 1.3 at 6 GPa, concluding that intratetrahedral J_4 antiferromagnetic coupling strengthens while $|D_4|$ weakens. D_4 interactions are reported to have the highest value of $|D/J|$ in Cu_2OSeO_3 [34] and hence we estimated the value of J/D^2 for D_4 and J_4 interactions. The value of J_4/D_4^2 increases from 0.14 at 0 GPa to 0.20 at 6 GPa, which contributes to enhance the JK/aD^2 parameter together with an increased anisotropy and decreased Cu-Cu distances and in turn increases the skyrmion pocket size. Also, the Heisenberg exchange interactions J_1, J_2, J_4, and J_5 increases with increasing pressure (Table III) causing the observed rise in the helimagnetic transition temperature T_C in earlier studies [23].

C. Pressure dependence of Raman vibrational modes

Factor group analysis of cubic ($P2_13$) Cu_2OSeO_3 yields 84 Raman-active phonon modes [42], among which 27 modes

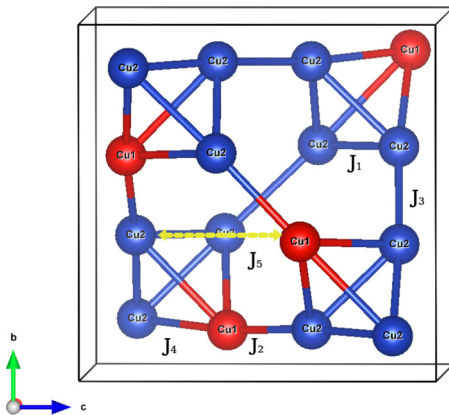FIG. 5. (a) Unit cell of Cu_2OSeO_3 (only Cu atoms are shown) with two types of copper atoms, Cu1 atoms with down-spin (red atoms) and Cu2 atoms with up-spins (blue atoms). J_1 and J_3 are ferromagnetic couplings, while J_2, J_4, and J_5 are antiferromagnetic exchange couplings. J_5 is the super-superexchange interaction. J_1 and J_4 are intratetrahedral and J_2 and J_3 are intertetrahedral couplings.

TABLE II. Estimated value of D and J parameters and the distance (d) between respective Cu-atoms.

Coupling	J (meV)	D (meV)	d (Å)
1.	−2.12	(0.53, 0.51, −0.08)	3.07
2.	12.46	(−2.64, −0.6, −2.13)	3.07
3.	−6.77	(−0.90, −0.61, −0.38)	3.27
4.	2.10	(0.89, 2.1, −3.17)	3.35
5.	2.54	(−0.12, 0.19, −0.09)	6.41

TABLE III. Pressure dependence of J-coupling constants. All J-couplings strengthen with pressure except J_3. Super-superexchange interaction J_5 shows a small increase from 0 to 6 GPa.

J (meV)	At 0 GPa	At 3 GPa	At 6 GPa
J_1	−2.12	−2.56	−2.99
J_2	12.46	12.53	12.66
J_3	−6.77	−6.60	−6.57
J_4	2.10	2.52	3.01
J_5	2.54	2.57	2.62

could be detected in our ambient Raman spectra in the frequency range 50–1300 cm^{-1}. Following the mode assignment by Miller *et al.* [43] and Kurnosov *et al.* [44] to the Raman and infrared-active phonons, the Raman spectra of Cu_2OSeO_3 can be divided into three distinct ranges of frequencies. While the low-frequency region (90–420 cm^{-1}) corresponds to the motion of the CuO_5 polyhedral entity, the modes in the frequency range 450–600 cm^{-1} can be attributed to the general motion of the oxygen atoms. The modes at frequency higher than 700 cm^{-1} bear vibrational fingerprints of SeO_3 units. Figure 6 depicts the effect of increasing pressure on the room-temperature Raman signal of Cu_2OSeO_3 in the range 30–950 cm^{-1}.

The highest pressure achieved in our high-pressure Raman measurements was 16.5 GPa. The ambient Raman spectra remained stable up to $\approx$5 GPa, above which significant changes started to appear in the scattering profile. The peak intensity
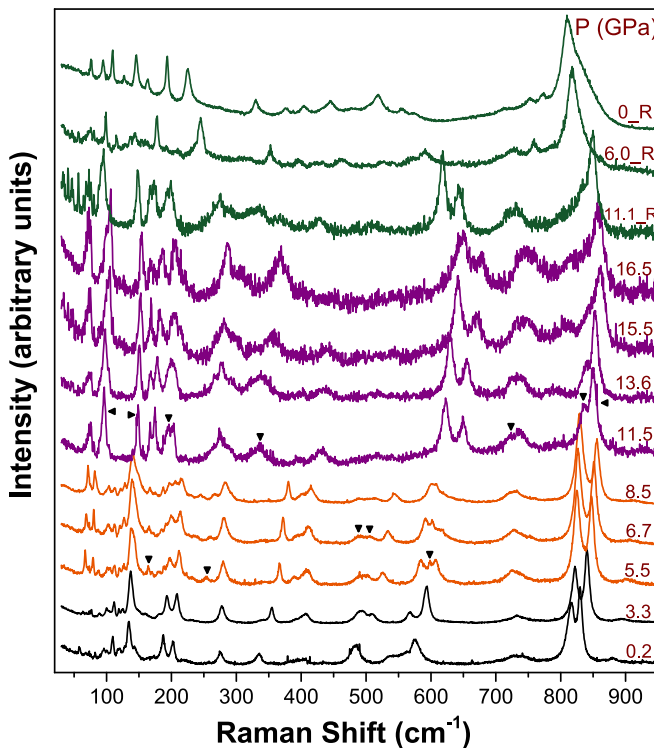

FIG. 7. Pressure evolution of selected phonon frequencies of Cu_2OSeO_3. Black solid circles denote phonon modes of the ambient cubic phase (shaded pink). New modes appearing at the onsets of the monoclinic (shaded yellow) and triclinic (shaded gray) transitions are denoted by blue and green solid circles, respectively. Solid lines are linear fits of phonon frequencies with pressure.

FIG. 6. Stacked Raman spectra of Cu_2OSeO_3 during pressurizing from 0.2 to 16.5 GPa (the top-most pattern is after depressurizing to ambient). Arrows indicate the emergence of new peaks at the onset of the monoclinic and triclinic phases.
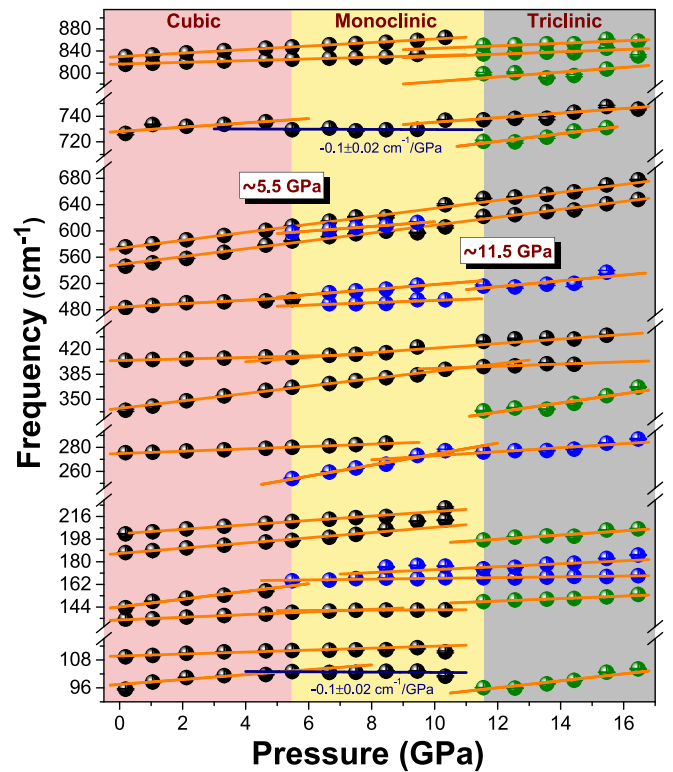
of the 546 cm^{-1} mode enhanced significantly along with disappearance of the 143 cm^{-1} mode and the emergence of three new phonons at $\approx$165, 254, and 598 cm^{-1} around 5.5 GPa followed by splitting of the 496 cm^{-1} mode into 489 and 506 cm^{-1} around 6.7 GPa. Appearance of new phonon modes in the Raman spectra confirms symmetry lowering [cubic ($P2_13$) to monoclinic ($P12_11$)] as established from our high-pressure XRD results. Structural evolution of the cubic phase into a monoclinic structure induces significant deformation in the CuO_5 polyhedral units, causing the development of new modes along with the vanishing of the old ones in the low-frequency band ($<$420 cm^{-1}). Also, the distortion in the Cu-O bond lengths and Cu-O-Cu bond angles rearranges the vibrational spectrum of the oxygen atoms, as reflected in the increasing intensity of the 546 cm^{-1} mode and splitting of the 496 cm^{-1} mode. The onset pressure for the transition is slightly lower for Raman measurements than that of XRD due to higher sensitivity of Raman scattering to probe any deformation of the crystal. Our Raman results also confirm the 11 GPa monoclinic ($P12_11$) to triclinic ($P1$) transition with the appearance of new Raman modes at $\approx$95, 138, 197, 334, 716, 786, 820, and 844 cm^{-1} as well as the disappearance of some of the existing modes around 11.5 GPa. Three top-most patterns of Fig. 6 represent spectra while releasing the pressure. The high-pressure phase is found to be stable down to 11.1 GPa, below which the spectrum transforms to

TABLE IV. Phonon mode frequencies, their pressure derivatives, and the corresponding Grüneisen parameters for ambient and high-pressure phases of Cu_2OSeO_3. Nonexistence of modes in regions are denoted by "NE."

Phase	ω (cm^{-1})	$\frac{d\omega}{dP}$ (cm^{-1}/GPa)			$\gamma_i = \frac{B_0}{\omega}\frac{d\omega}{dP}$
		I	II	III	
	95.4 ± 0.3	1.0 ± 0.2	-0.1 ± 0.02	NE	0.8
	109.3 ± 0.05		0.4 ± 0.06	NE	0.3
	134.2 ± 0.05	1.0 ± 0.05	0.1 ± 0.04	NE	0.5
	143.5 ± 0.3	3.1 ± 0.5	NE	NE	1.6
	187.3 ± 0.05		2.1 ± 0.1	NE	0.8
	202.2 ± 0.06		1.7 ± 0.05	NE	0.6
	275.6 ± 0.1		1.0 ± 0.03	NE	0.3
Cubic (I)	334.5 ± 0.2		5.2 ± 0.1	1.5 ± 0.5	1.1
($B_0 = 74.5$ GPa)	404.6 ± 0.6	1.0 ± 0.1	3.2 ± 0.3		0.2
	483.4 ± 0.1	2.7 ± 0.5	NE	NE	0.4
	546.2 ± 0.5		6.0 ± 0.1		0.8
	575.8 ± 0.1		6.1 ± 0.2		0.8
	726.5 ± 1.0	1.7 ± 0.3	-0.1 ± 0.02	1.6 ± 0.3	0.2
	815.8 ± 0.04		1.5 ± 0.04	NE	0.1
	830.1 ± 0.02		3.2 ± 0.05	NE	0.3
	164.9 ± 0.2	NE	0.3 ± 0.04		0.3
Monoclinic (II)	175.8 ± 0.4	NE	1.2 ± 0.3		1.1
($B_0 = 161.1$	253.9 ± 0.3	NE	4.6 ± 0.3	1.7 ± 0.3	2.9
GPa)	489.1 ± 0.6	NE	1.7 ± 0.4	NE	0.5
	506.0 ± 0.7	NE	3.8 ± 0.5	NE	1.2
	597.9 ± 0.2	NE	3.6 ± 0.1	4.4 ± 1.7	1.0
	96.1 ± 0.06	NE	NE	1.5 ± 0.3	2.9
	148.3 ± 0.06	NE	NE	1.0 ± 0.1	1.2
Triclinic (III)	197.4 ± 0.2	NE	NE	1.6 ± 0.3	1.5
($B_0 = 183.3$	333.7 ± 0.5	NE	NE	6.4 ± 1.5	3.5
GPa)	720.3 ± 0.9	NE	NE	3.0 ± 0.3	0.8
	799.0 ± 2.3	NE	NE	1.8 ± 0.4	0.4
	834.6 ± 0.2	NE	NE	2.1 ± 1.0	0.5
	850.2 ± 0.1	NE	NE	2.3 ± 0.4	0.5

a completely different profile with sharp well-defined Raman modes not matching either to any of the two high-pressure phases or the initial ambient one, establishing that, during decompression, the system takes a disparate structural transformation pathway to the metastable monoclinic phase as established by our XRD results. Group theory predicts a total of 36 Raman-active modes ($\Gamma_{\text{Raman}} = 18A_g + 18B_g$) for this pressure-released monoclinic structure, among which we have observed 22 modes in the frequency range 30–950 cm^{-1}. The highly dissimilar spectral layout of this phase compared with that of the other phases of this system (ambient cubic, high-pressure monoclinic, and triclinic) confirms the unique polyhedral configuration of this pressure-released monoclinic structure.

All the Raman modes have been fit with Lorentzian profiles and the mode frequencies are plotted against pressure in Fig. 7. The straight lines represent fitting of mode frequencies using the linear equation $\omega_P = \omega_0 + (\frac{d\omega}{dP})P$. The frequencies of phonon modes, their $\frac{d\omega}{dP}$ values in different phases, and the

corresponding Grüneisen parameters $\gamma_i = \frac{B_0}{\omega}\frac{d\omega}{dP}$ are listed in Table IV. All the modes exhibit normal hardening behavior with increasing pressure, as expected due to pressure enhancement of stiffness constant due to shrinkage of the unit cell. Figure 7 features the two structural transitions in Cu_2OSeO_3 at ≈ 5 and ≈ 11 GPa with new modes appearing (indicated by blue and green solid circles) and alteration of the slopes of the phonon modes across the transition pressures. The two high-pressure phases are associated with positive slope values for the phonon modes except for the two modes at ≈ 95 and 726 cm^{-1} associated with the initial cubic phase showing mild softening with a slightly negative slope of -0.1 ± 0.02 cm^{-1}/GPa (indicated by navy blue solid lines) in the pressure range 5–10 GPa.

IV. CONCLUSION

To summarize, structural and vibrational properties of chiral B20 magnet Cu_2OSeO_3 has been investigated at room

temperature under high pressure using x-ray diffraction and Raman-scattering studies. The ambient cubic phase ($P2_13$, #198) transforms to monoclinic ($P12_11$, #4) at ≈ 7 GPa and to triclinic ($P1$, #1) at ≈ 11 GPa both the transitions being first order. The transitions are path dependent in nature and the system adopts another monoclinic structure ($P12_1/c1$, #14) up on decompressing back to ambient. It would be interesting to calculate magnetic exchange interactions in this pressure-released new monoclinic structure based on our observed structural parameters. The interatomic distances of the copper tetrahedra falls off with increasing pressure in the cubic phase and is responsible for the increasing T_C value as well as the growing pocket size of the skyrmion phase. High-pressure Raman studies support the two structural transitions with emergence of new vibrational modes in the spectra and changes in pressure derivative of the phonon frequencies across the transition pressures. Our first-principles calculations for the ambient cubic phase ($P2_13$, #198) reveal that hydrostatic pressure affects spin-spin exchange interactions significantly, and pressure is likely to enhance the size of skyrmion pocket in Cu_2OSeO_3. These observations should open up future scope for detailed theoretical and experimental studies to unleash the microscopic magnetic configurations of these new high-pressure structures of Cu_2OSeO_3.

[1] S. Seki, X. Z. Yu, S. Ishiwata, and Y. Tokura, Science **336**, 198 (2012).

[2] E. Ruff, P. Lunkenheimer, A. Loidl, H. Berger, and S. Krohns, Sci. Rep. **5**, 15025 (2015).

[3] S. Mühlbauer, B. Binz, F. Jonietz, C. Pfleiderer, A. Rosch, A. Neubauer, R. Georgii, and P. Böni, Science **323**, 915 (2009).

[4] Y. Ishikawa and M. Arai, J. Phys. Soc. Jpn. **53**, 2726 (1984).

[5] S. V. Grigoriev, V. A. Dyadkin, D. Menzel, J. Schoenes, Yu. O. Chetverikov, A. I. Okorokov, H. Eckerlebe, and S. V. Maleyev, Phys. Rev. B **76**, 224424 (2007).

[6] M. Uchida, N. Nagaosa, J. P. He, Y. Kaneko, S. Iguchi, Y. Matsui, and Y. Tokura, Phys. Rev. B **77**, 184402 (2008).

[7] U. K. Rößler, A. N. Bogdanov, and C. Pfleiderer, Nature (London) **442**, 797 (2006).

[8] N. Nagaosa and Y. Tokura, Nat. Nanotechnol. **8**, 899 (2013).

[9] X. Z. Yu, Y. Onose, N. Kanazawa, J. H. Park, J. H. Han, Y. Matsui, N. Nagaosa, and Y. Tokura, Nature (London) **465**, 901 (2010).

[10] S. V. Grigoriev, V. A. Dyadkin, E. V. Moskvin, D. Lamago, T. Wolf, H. Eckerlebe, and S. V. Maleyev, Phys. Rev. B **79**, 144417 (2009).

[11] S. Heinze, K. von Bergmann, M. Menzel, J. Brede, A. Kubetzka, R. Wiesendanger, G. Bihlmayer, and S. Blügel, Nat. Phys. **7**, 713 (2011).

[12] X. Z. Yu, N. Kanazawa, Y. Onose, K. Kimoto, W. Z. Zhang, S. Ishiwata, Y. Matsui, and Y. Tokura, Nat. Mater. **10**, 106 (2011).

[13] G. Meunier and M. Bertaud, J. Appl. Crystallogr. **9**, 364 (1976).

[14] J. Romhanyi, J. van den Brink, and I. Rousochatzakis, Phys. Rev. B **90**, 140404(R) (2014).

[15] T. Adams, A. Chacon, M. Wagner, A. Bauer, G. Brand, B. Pedersen, H. Berger, P. Lemmens, and C. Pfleiderer, Phys. Rev. Lett. **108**, 237204 (2012).

[16] C. Pfleiderer, P. Böni, T. Keller, U. K. Rößler, and A. Rosch, Science **316**, 1871 (2007).

[17] N. Martin, M. Deutsch, J.-P. Itié, J.-P. Rueff, U. K. Rößler, K. Koepernik, L. N. Fomicheva, A. V. Tsvyashchenko, and I. Mirebeau, Phys. Rev. B **93**, 214404 (2016).

[18] A. Barla, H. Wilhelm, M. K. Forthaus, C. Strohm, R. Rüffer, M. Schmidt, K. Koepernik, U. K. Rößler, and M. M. Abd-Elmeguid, Phys. Rev. Lett. **114**, 016803 (2015).

[19] M. K. Forthaus, G. R. Hearne, N. Manyala, O. Heyer, R. A. Brand, D. I. Khomskii, T. Lorenz, and M. M. Abd-Elmeguid, Phys. Rev. B **83**, 085101 (2011).

[20] S. Guo, J. Wang, H. Du, C. Lu, C. Zhang, and Z. Lu, Comput. Mater. Sci. **142**, 285 (2018).

[21] G. A. Valkovskiy, E. G. Yashina, V. A. Dyadkin, A. V. Tsvyashchenko, L. N. Fomicheva, M. Bykov, E. Bykova, L. Dubrovinsky, D. Y. Chernyshov, and S. V. Grigoriev, J. Phys.: Condens. Matter **29**, 085401 (2007).

[22] H. Wilhelm, M. Schmidt, R. Cardoso-Gil, U. Burkhardt, M. Han, U. Schwarz, and L. Akselrud, Sci. Tech. Adv. Mater. **8**, 416 (2007).

[23] V. A. Sidorov, A. E. Petrova, P. S. Berdonosov, V. A. Dolgikh, and S. M. Stishov, Phys. Rev. B **89**, 100403(R) (2014).

[24] I. Levatić, P. Popčević, V. Šurija, A. Kruchkov, H. Berger, A. Magrez, J. S. White, H. M. Rønnow, and I. Živković, Sci. Rep. **6**, 21347 (2016).

[25] L. Deng, H.-C. Wu, A. P. Litvinchuk, N. F. Q. Yuan, J.-J. Lee, R. Dahal, H. Bergerf, H.-D. Yang, and C.-W. Chu, Proc. Natl. Acad. Sci. USA **117**, 8783 (2020).

[26] J.-W. G. Bos, C. V. Colin, and T. T. M. Palstra, Phys. Rev. B **78**, 094416 (2008).

[27] G. J. Piermarini, S. Block, and J. D. Barnett, J. Appl. Phys. **44**, 5377 (1973).

[28] H. Mao, J. Xu, and P. Bell, J. Geophys. Res. **91**, 4673 (1986).

[29] A. Hammersley, *Computer Program FIT2D* (ESRF, Grenoble, 1998).

[30] A. C. Larson and R. B. Von Dreele, GSAS General Structure Analysis System, Los Alamos Natl. Laboratory Report No. LAUR 2000, 86-748.

[31] R. J. Angel, M. Bujak, J. Zhao, G. D. Gattac, and S. D. Jacobsen, J. Appl. Crystallogr. **40**, 26 (2007).

[32] H. Effenberger and F. Pertlik, Monatsh. Chem. **117**, 887 (1986).

[33] F. Birch, J. Geophys. Res. **91**, 4949 (1986).

[34] J. H. Yang, Z. L. Li, X. Z. Lu, M.-H. Whangbo, Su-Huai Wei, X. G. Gong, and H. J. Xiang, Phys. Rev. Lett. **109**, 107203 (2012).

[35] O. Janson, I. Rousochatzakis, A. A. Tsirlin, M. Belesi, A. A. Leonov, U. K. Rößler, J. van den Brink, and H. Rosner, Nat. Commun. **5**, 5376 (2014).

[36] G. Kresse and J. Furthmüller, Comput. Mater. Sci. **6**, 15 (1996).

[37] G. Kresse and J. Furthmüller, Phys. Rev. B **54**, 11169 (1996).

[38] A. I. Liechtenstein, V. I. Anisimov, and J. Zaanen, Phys. Rev. B **52**, R5467(R) (1995).

[39] J. P. Perdew, J. A. Chevary, S. H. Vosko, K. A. Jackson, M. R. Pederson, D. J. Singh, and C. Fiolhais, Phys. Rev. B **46**, 6671 (1992).

[40] P. E. Blöchl, Phys. Rev. B **50**, 17953 (1994).

[41] H. J. Xiang, E. J. Kan, Su-Huai Wei, M.-H. Whangbo, and X. G. Gong, Phys. Rev. B **84**, 224429 (2011).

[42] V. P. Gnezdilov, K. V. Lamonova, Yu. G. Pashkevich, P. Lemmens, H. Berger, F. Bussy, and S. L. Gnatchenko, Low Temp. Phys. **36**, 550 (2010).

[43] K. H. Miller, X. S. Xu., H. Berger, E. S. Knowles, D. J. Arenas, M. W. Meisel, and D. B. Tanner, Phys. Rev. B **82**, 144107 (2010).

[44] V. S. Kurnosov, V. P. Gnezdilov, V. V. Tsapenko, P. Lemmens, and H. Berger, Low Temp. Phys. **38**, 489 (2012).

[45] P. Lotti, S. Milani, M. Merlini, B. Joseph, F. Alabarse, and A. Lausi, J. Synchrotron Radiat. **27**, 222 (2020).